J. Fluid Mech. (2018), *vol.* 841, *pp.* 614–635.
doi:10.1017/jfm.2018.107

Damping of quasi-two-dimensional internal wave attractors by rigid-wall friction

F. Beckebanze[1,†], C. Brouzet[2], I. N. Sibgatullin[3,4,5] and L. R. M. Maas[6]

[1]Mathematical Institute, Utrecht University, P.O. Box 80010, 3508 TA Utrecht, The Netherlands

[2]Univ Lyon, ENS de Lyon, Univ Claude Bernard, CNRS, Laboratoire de Physique, F-69342 Lyon, France

[3]Department of Mechanics and Mathematics, Moscow State University, Moscow 119191, Russia

[4]Institute for System Progamming, Moscow 109004, Russia

[5]Shirshov Institute of Oceanology, Moscow 117997, Russia

[6]Institute for Marine and Atmospheric Research Utrecht (IMAU), Utrecht University, Princetonplein 5, 3584 CC Utrecht, The Netherlands

(Received 25 July 2017; revised 22 November 2017; accepted 22 January 2018; first published online 26 February 2018)

The reflection of internal gravity waves at sloping boundaries leads to focusing or defocusing. In closed domains, focusing typically dominates and projects the wave energy onto 'wave attractors'. For small-amplitude internal waves, the projection of energy onto higher wavenumbers by geometric focusing can be balanced by viscous dissipation at high wavenumbers. Contrary to what was previously suggested, viscous dissipation in interior shear layers may not be sufficient to explain the experiments on wave attractors in the classical quasi-two-dimensional trapezoidal laboratory set-ups. Applying standard boundary layer theory, we provide an elaborate description of the viscous dissipation in the interior shear layer, as well as at the rigid boundaries. Our analysis shows that even if the thin lateral Stokes boundary layers consist of no more than 1 % of the wall-to-wall distance, dissipation by lateral walls dominates at intermediate wave numbers. Our extended model for the spectrum of three-dimensional wave attractors in equilibrium closes the gap between observations and theory by Hazewinkel *et al.* (J. Fluid Mech., vol. 598, 2008, pp. 373–382).

Key words: boundary layer structure, geophysical and geological flows, internal waves

1. Introduction

The dispersion relation of internal waves is given by $\omega_0^2 = N_0^2 \sin^2\theta$, with ω_0 the wave frequency, θ the angle of phase propagation with respect to the vertical, z the direction antiparallel to gravity and N_0 the Brunt–Väisälä frequency, here assumed constant. The group propagation is always orthogonal to the phase propagation (Sutherland 2010), thus θ also represents the angle of energy propagation with respect to the horizontal plane, and is fixed for monochromatic waves. This property results in geometric focusing or defocusing upon reflection at a sloping topography. Repeated

†Email address for correspondence: f.beckebanze@uu.nl

geometric focusing in closed domains can project the wave energy onto closed orbits, known as wave attractors (Maas & Lam 1995; Maas *et al.* 1997). In the vicinity of internal wave attractors, energy is dissipated by viscous dissipation (Hazewinkel *et al.* 2008), or lost to nonlinear wave–wave interactions (Scolan, Ermanyuk & Dauxois 2013; Brouzet *et al.* 2016*a*, 2017*a*; Dauxois *et al.* 2018). Internal wave attractors are studied most thoroughly in the classical quasi-two-dimensional trapezoidal set-ups (Maas & Lam 1995; Maas *et al.* 1997; Maas 2005, 2009; Swart *et al.* 2007; Grisouard, Staquet & Pairaud 2008; Harlander 2008; Hazewinkel *et al.* 2008, 2010; Scolan *et al.* 2013; Brouzet *et al.* 2016*a*,*b*, 2017*a*,*b*), geometries which are also popular in studies on closely related inertia wave attractors (Manders & Maas 2003; Klein *et al.* 2014; Troitskaya 2017). Recent studies also examine internal wave attractors confined to more sophisticated domains, resembling simplified ocean topography (Tang & Peacock 2010; Echeverri *et al.* 2011; Hazewinkel, Maas & Dalziel 2011; Wang *et al.* 2015; Guo & Holmes-Cerfon 2016). Applying standard boundary layer theory, Klein *et al.* (2014) establish the importance of the Ekman boundary layers for inertial wave attractors. Surprisingly, the role of energy dissipation at rigid boundaries for internal wave attractors still remains an open question, even for the simplest domain, the classical quasi-two-dimensional (quasi-2-D) trapezoid. The energy loss at the wave attractor – and in the broader sense internal wave beams – can have far-reaching consequences for the mixing budget of stratified fluids, such as the deep oceans (Wunsch & Ferrari 2004) and marginal seas (Lamb 2014).

In this paper, we apply standard boundary layer theory to quantify the frictional damping mechanisms of internal wave attractors in the classical quasi-2-D laboratory set-up. Frictional dissipation takes place in two types of viscous layers: the shear layers in the interior along the attractor and the boundary layers at the rigid boundaries.

Internal wave damping through interior shear layers, first described by Thomas & Stevenson (1973), has been studied extensively over the past decades, and in particular in the context of internal wave attractors by Dintrans, Rieutord & Valdettaro (1999), Swart (2007), Hazewinkel *et al.* (2008), Brouzet *et al.* (2016*a*) and inertial wave attractors by Dintrans *et al.* (1999), Rieutord, Georgeot & Valdettaro (2001, 2002), Ogilvie (2005), Jouve & Ogilvie (2014). A simple model for an equilibrium wave attractor spectrum, with the energy input at the basin scale (low wavenumbers) and dissipation only through internal shear at high wavenumbers, has been derived by Hazewinkel *et al.* (2008). Although the structure of their theoretical spectrum resembles their experimentally observed spectrum of an internal wave attractor in the classical quasi-2-D trapezoidal set-up, the discrepancy hints at significant dissipation at the rigid boundaries. Grisouard *et al.* (2008) performed 2-D numerical simulations, designed to replicate the laboratory experiment by Hazewinkel *et al.* (2008) with free-slip boundaries. Their simulations underestimates the energy dissipation at high wavenumbers, also indicating an additional energy sink at the walls in the laboratory. The fully 3-D simulations by Brouzet *et al.* (2016*b*) signify significantly increased dissipation rates in the lateral boundary layers. Our theoretical analysis shows that adding dissipation at the rigid boundaries closes the gap between the model and observations in Hazewinkel *et al.* (2008).

Stokes boundary layers in homogenous fluids are well understood and are described in many text books on fluid mechanics, e.g. Schlichting & Gersten (2000). The stratified boundary layers for monochromatic internal waves are to some extent analogous to homogenous Stokes boundary layers, but differ in a number of

fundamental aspects, such as the characteristic thickness of the boundary layer. The thickness of the stratified boundary layer is given by

$$d_0 = \mu^{-1}\left(\frac{\nu}{\omega}\right)^{1/2}, \quad \text{with } \mu = \sqrt{\left|\frac{\sin^2\varphi}{\sin^2\theta} - 1\right|} \tag{1.1}$$

dependent on the angle φ of the boundary (with respect to the horizontal) and the internal wave inclination, θ. Note that horizontal boundaries ($\varphi = 0$), investigated by Renaud & Venaille (2018), coincide with the homogeneous case, $\mu = 1$. For near-critical reflections ($\varphi \sim \theta$) the boundary layer thickness d_0 tends to infinity, making different approaches, such as in Dauxois & Young (1999), necessary. The theoretical investigation on stratified rotating boundary layers by Swart *et al.* (2010) stresses the importance of these critical cases ($\varphi \sim \theta$) for the generation of internal inertia waves by oscillating boundaries. Kistovich & Chashechkin (1995*a*,*b*) computed the boundary layer of a reflecting internal wave beam, but did not account for the dissipative energy loss inside the boundary layer. Vasiliev & Chashechkin (2003) constructed asymptotic solutions for internal wave fields generated by a rigid plane vibrating along its surface. We now investigate a situation in which the energy flux is in opposite direction, i.e. the wave attractor loses energy to the rigid walls. The objective is to understand and quantify the damping induced by stratified boundary layers on wave attractors. Partial results are also reported in Beckebanze & Maas (2016).

The structure of this paper is as follows. The formulation of the problem is described in § 2. In § 3, we construct inviscid wave attractor solutions. Internal shear, lateral wall boundary layers and boundary layers at the reflecting walls are subsequently added in respectively §§ 4–6. In § 7, we compare our extended model for the equilibrium wave attractor spectrum with the laboratory experiment and 3-D simulations. Conclusions are drawn in § 8.

2. Preliminaries

In this paper we consider monochromatic internal waves in a linearly stratified Boussinesq fluid inside a trapezoidal tank

$$D = \{(x, y, z) \in \mathbb{R} | -l_y \leqslant y \leqslant l_y, -l_x \leqslant x \leqslant l_x, 0 \leqslant z \leqslant \min[h, (l_x - x)\tan\alpha]\}, \tag{2.1}$$

with z antiparallel to gravity. We anticipate ratios $\sin\theta = \omega_0/N_0$ of wave frequency ω_0 over Brunt–Väisälä frequency N_0, such that the internal wave motion is predominantly confined to a neighbourhood around the theoretical inviscid wave attractor, as illustrated in figure 1(*a*,*b*). The Cartesian coordinates, (x, y, z), are dimensionalized with the length scale λ_0, which we assume to be the characteristic wavelength of the predominant wave motion – the viscous wave attractor – measured in the cross-beam direction. Note that scaling the non-dimensional half-bottom-length, l_x, half-width, l_y, and height, h, with the same length scale, λ_0, leaves the angle of the inclined wall, α, and the energy propagation angle, θ, both with respect to the horizontal, invariant. We require $l_y \gtrapprox 1$, i.e. the dimensional width, $W = 2l_y\lambda_0$, is at least of the same order of magnitude as the wave attractor cross-beam length scale, λ_0.

We consider sufficiently weak monochromatic forcing, generating only small-amplitude wave motion. This means that the Stokes number, $U_0/\omega_0\lambda_0$, with U_0 the dimensional scale of the internal wave velocity, is small such that all nonlinear advection terms can be neglected.

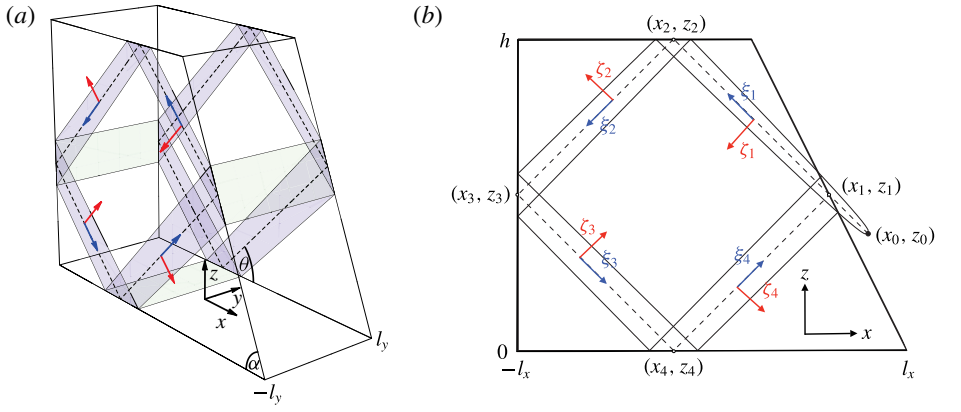

FIGURE 1. (Colour online) Schematic view of the 3-D trapezoidal domain D (a), and its side view (b). The viscous wave attractor interacts with the rigid boundaries of D (free slip at surface, $z = h$) primarily in the shaded areas (a), as it is confined to a region around the theoretical inviscid wave attractor orbit (dashed lines in a,b). The black dot in (b) to the right of the inclined wall indicates the virtual source. The phase propagation is along coordinates ζ_n, $n = 1, 2, 3, 4$ (red arrows), whereas the energy propagation is along ξ_n (blue arrows) at an angle θ with respect to the horizontal x. The thickening of the wave attractor in the energy propagation direction is due to viscous damping, as discussed in § 5, and it is balanced by the focusing reflection at inclined wall with angle α.

Under these assumptions, the (linearized) equations governing the dimensionless velocity field $\boldsymbol{u} = (u, v, w)$, buoyancy b and pressure p of the Boussinesq fluid, with scaled Brunt–Väisälä frequency $N = N_0/\omega_0 = \pm 1/\sin\theta$, are given in subscript-derivative notation by

$$\boldsymbol{u}_t = -\boldsymbol{\nabla} p + b\hat{\boldsymbol{z}} + \delta^2 \Delta \boldsymbol{u} + \boldsymbol{f}\,\mathrm{e}^{-it}, \quad b_t = -N^2 w, \quad \boldsymbol{\nabla}\cdot\boldsymbol{u} = 0. \tag{2.2a,b}$$

Here, $\delta = d_0/\lambda_0 \ll 1$ is the non-dimensional Stokes boundary layer width, with $d_0 = \sqrt{\nu/\omega_0}$, and ν the kinematic viscosity constant. We assume the fluid to be salt stratified, and neglect diffusivity by considering an infinite Schmidt number (ratio of kinematic viscosity over mass diffusivity, typically approximately 700 for salt-stratified fluids). The forcing $\boldsymbol{f} = \boldsymbol{f}(x, z)$ is assumed to be uniform in the transverse y-direction. For mathematical convenience, we consider $\boldsymbol{f}$ to be a localized source, located outside the trapezoidal domain, D, as illustrated in figure 1(b). This enables us to describe the viscous wave attractor as four branches of a viscous internal wave beam (Ogilvie 2005). The downside of this approach is a slight violation of the impermeability boundary condition at the inclined wall near the wave attractor upon incorporating viscous attenuation. In fact, the energy input into the closed domain D occurs through spatially non-uniform oscillations at the inclined wall, on which we have no control *a priori*. We accept this disadvantage, which also underlies the theoretical 2-D spectra by Hazewinkel *et al.* (2008), because it is irrelevant for the energy loss through the boundary layers of a quasi-2-D weakly viscous wave attractor – the main objective of the presented analysis.

We solve the governing equations (2.2) asymptotically with no-slip boundary conditions, $\boldsymbol{u} = 0$, at the boundary of the trapezoidal domain D (except at the free surface, $z = h$, where we impose free slip), by expanding the velocity vector $\boldsymbol{u}$ in the

small parameter δ,

$$\boldsymbol{u} = \boldsymbol{u}_0 + \delta \boldsymbol{u}_1 + O(\delta^2), \tag{2.3}$$

and similarly for buoyancy b and pressure p. We start in § 3 by solving (2.2) at $O(\delta^0)$ with free-slip boundary conditions for $\boldsymbol{u}_0$. Free slip means that we only require the normal derivative of tangential velocity to vanish. Viscous attenuation is added in § 4, and in § 5, we extend $\boldsymbol{u}_0$ such that it vanishes at the lateral walls (surfaces along dashed theoretical attractor in figure 1(*a*), blue online). In § 6, we add correction terms in order to satisfy the no-slip boundary condition also at the reflection sides (green surfaces in figure 1(*a*), green online).

3. Wave attractor branches in interior

It is convenient to express the four wave attractor branches in the rotated and shifted coordinates $[\xi_n, \zeta_n]$, $n = 1, 2, 3, 4$, given by

$$\begin{bmatrix} \xi_{1,3} \\ \zeta_{1,3} \end{bmatrix} = \mp \begin{bmatrix} \cos\theta & -\sin\theta \\ \sin\theta & \cos\theta \end{bmatrix} \begin{bmatrix} x - x_{1,3} \\ z - z_{1,3} \end{bmatrix}, \quad \begin{bmatrix} \xi_{2,4} \\ \zeta_{2,4} \end{bmatrix} = \mp \begin{bmatrix} \cos\theta & \sin\theta \\ \sin\theta & -\cos\theta \end{bmatrix} \begin{bmatrix} x - x_{2,4} \\ z - z_{2,4} \end{bmatrix}, \tag{3.1a,b}$$

with $[x_n, z_n]$ the reflection points of the attractor, see figure 1(*b*). The theoretical inviscid wave attractor (dashed lines in figure 1) corresponds to $\zeta_n = 0$, for $n = 1, 2, 3, 4$.

The inviscid $O(\delta^0)$-velocity field generated by a monochromatic, localized source, describing the first wave attractor branch (labelled with the super-script 1), can be written as

$$\boldsymbol{u}_0^{[1]} = \hat{\boldsymbol{\xi}}_1 U(\zeta_1) = [-\cos\theta, 0, \sin\theta]\, U(\zeta_1), \quad U(\zeta) = \int_0^\infty \hat{U}(k) \exp[\mathrm{i}(k\zeta - t)]\, \mathrm{d}k, \tag{3.2}$$

where k is the non-dimensional wavenumber (scaled by λ_0^{-1}). Physical quantities are always the real part of the presented expression, and the hat on a coordinate always denotes the unit vector pointing in the direction of this coordinate, i.e. $\hat{\boldsymbol{\xi}}_1$ is the unit vector along the first wave attractor branch. The Fourier spectrum

$$\hat{U}(k) = \frac{1}{2\pi} \int_{-\infty}^{\infty} U(\zeta) \exp[-\mathrm{i}\zeta k]\, \mathrm{d}\zeta \tag{3.3}$$

of the along-wave-beam velocity component U depends on the unspecified localized source at (x_0, z_0). The main objective of the presented analysis is to derive constraints for $\hat{U}(k)$, based on geometric wave focusing (this section), and viscous dissipation (§§4–6). Note that $\hat{U}(k) = 0$ for $k \leqslant 0$ because no energy can propagate towards the source (by assumption).

Subsequent free-slip reflections of the first wave attractor branch at the surface, $z = h$, at the vertical wall, $x = -l_x$, and at the bottom, $z = 0$, lead to the following velocity fields for the second, third and fourth wave attractor branches:

$$\boldsymbol{u}_0^{[n]} = \hat{\boldsymbol{\xi}}_n U(\zeta_n) \quad \text{for } n = 2, 3, 4. \tag{3.4}$$

The fourth branch returns to the inclined wall, $z = (l_x - x)\tan\alpha$, where the free-slip boundary condition reads

$$\mathrm{Re}\left[\left(\boldsymbol{u}_0^{[1]} + \boldsymbol{u}_0^{[4]}\right) \cdot \hat{\boldsymbol{n}}_\alpha\right] = 0, \tag{3.5}$$

with $\hat{\boldsymbol{n}}_\alpha = [\sin\alpha, 0, \cos\alpha]$ a normal vector of the inclined wall. On the inclined wall, $z = (l_x - x)\tan\alpha$, we have

$$\boldsymbol{u}_0^{[1]} \cdot \hat{\boldsymbol{n}}_\alpha = -\sin[\alpha - \theta] \int_0^\infty \hat{U}(k) \exp\left[ik\frac{\sin[\alpha-\theta]}{\cos\alpha}(x - x_1) - it\right] \mathrm{d}k \tag{3.6}$$

and

$$\boldsymbol{u}_0^{[4]} \cdot \hat{\boldsymbol{n}}_\alpha = \sin[\alpha + \theta] \int_0^\infty \hat{U}(k) \exp\left[ik\frac{\sin[\alpha+\theta]}{\cos\alpha}(x - x_1) - it\right] \mathrm{d}k. \tag{3.7}$$

Substitution of $k \to \gamma k$ in (3.6), with

$$\gamma = \frac{\sin[\alpha + \theta]}{\sin[\alpha - \theta]}, \tag{3.8}$$

such that the exponential terms in (3.6) and (3.7) become identical, and inserting (3.6) and (3.7) into (3.5) gives

$$\mathrm{Re}\left[\int_0^\infty (\hat{U}(\gamma k) - \hat{U}(k)) \exp\left[ik\frac{\sin[\alpha+\theta]}{\cos\alpha}(x - x_1) - it\right] \mathrm{d}k\right] = 0. \tag{3.9}$$

Satisfying the free-slip boundary conditions at the four reflecting walls for all times t thus imposes the spectral constraint

$$\hat{U}(\gamma k) = \hat{U}(k). \tag{3.10}$$

Solutions to this functional equation are non-unique (see Beckebanze & Keady 2016, pp. 185–186 for a more rigorous analysis of this functional equation). The non-uniqueness is apparent by writing $\hat{U}(k) = P(\log_\gamma(k))$, which satisfies (3.10) for arbitrary function P with period 1: $\hat{U}(\gamma k) = P(\log_\gamma(\gamma k)) = P(1 + \log_\gamma(k)) = P(\log_\gamma(k)) = \hat{U}(k)$. For all these spectra (except $P = 0$) the velocity expressions (3.2) and (3.4) are non-integrable for points on the inviscid wave attractor, $\zeta_n = 0$ (dashed lines in figure 1*b*), confirming the results by Rieutord *et al.* (2001). The exact self-similar wave attractor solution by Maas (2009) in terms of countable infinite Fourier coefficients is an example of such spectrum $\hat{U}(k)$ (where P is a superposition of Dirac delta functions). The self-similar structure of wave attractors is reflected by the $\log_\gamma$-periodicity of the spectra. Next, we regularize the singularity on the inviscid wave attractor by adding viscous attenuation.

4. Internal shear layer dissipation

Incorporating weak viscous attenuation in an asymptotic wave beam expression was first done by Thomas & Stevenson (1973), and has been achieved using different procedures (see §6 of Voisin (2003) for an overview). Here, we determine the effect of viscosity on the spectrum $\hat{U}(k)$ – an exponential attenuation factor – and incorporate it in the inviscid spectral decompositions for the velocity field, (3.2) and (3.4). We briefly demonstrate this analysis because of its similarity with the damping mechanisms caused by the rigid walls, presented in §§ 5 and 6.

For notational convenience, we drop the superscript $[n]$, and consider a wave attractor branch with velocity U in the along-energy-propagation direction ξ, and

phase propagation along ζ. Upon incorporating continuity and buoyancy equations, one can write the governing equation for U as

$$-\Delta U + N^2\left(\sin^2\theta\ U_{\zeta\zeta} + 2\cos\theta\sin\theta U_{\zeta\xi} + \cos^2\theta U_{\xi\xi}\right) = -\mathrm{i}\delta^2\Delta^2 U. \tag{4.1}$$

This equation is solved at $O(\delta^0)$ by $U(\zeta)$ as defined in (3.2), provided the non-dimensional dispersion relation, $1 = N^2\sin^2\theta$, holds. The velocity function U is still an $O(\delta^0)$-solution if we let the spectrum $\hat{U}(k)$ to be weakly dependent on the along-beam coordinate ξ, that is to say, if $\hat{U}_\xi \in O(\delta)$. We assume $\hat{U}_\xi \in O(\delta^2) \subset O(\delta)$. Equation (4.1) at $O(\delta^2)$ then becomes

$$2N^2\sin\theta\cos\theta U_{\zeta\xi} = -\mathrm{i}\delta^2 U_{\zeta\zeta\zeta\zeta}. \tag{4.2}$$

This is solved by

$$U = \int_0^\infty \hat{U}(k,\xi)\exp\left[\mathrm{i}k\zeta - \mathrm{i}t\right]\,\mathrm{d}k, \quad \hat{U}(k,\xi) = \hat{U}(k)\exp\left[-\delta^2\frac{\tan\theta}{2}k^3(\xi-\xi_0)\right], \tag{4.3}$$

for arbitrary $\hat{U}(k)$, and where ξ_0 is the along-wave-attractor distance to the virtual localized source. Adding weak viscous attenuation to the 2-D wave attractor velocity field is thus achieved by replacing $\hat{U}(k) \to \hat{U}(k)\exp\left[-\delta^2(\tan\theta/2)k^3(\xi-\xi_0)\right]$ in the velocity fields (3.2) and (3.4).

Note that the real (imaginary) part $U(\zeta, \xi)$ in (4.3) is even (odd) in ζ around $\zeta = 0$. This symmetry is preserved among reflections at horizontal or vertical boundaries, whereas reflections at inclined boundaries break it. All attractors include symmetry-breaking reflections, hence, their velocity fields cannot be symmetric around the inviscid attractor orbit, $\zeta = 0$, when including viscous attenuation. Describing the wave attractor branches nevertheless by a viscous wave beam emitted from a virtual point source leads to a slight violation of the impermeability boundary condition at the inclined wall. Instead, the viscous wave attractor satisfies an oscillating boundary constraint at the inclined wall, with the spatial scale of the wall oscillation corresponding to the cross-beam thickness. Physically, the internal waves are thus generated by spatially non-uniform oscillations of the inclined wall.

Incorporating the viscous attenuation in the impermeability constraint (3.9) at the reflection point (x_1, z_1) results in the modified spectral constraint

$$\hat{U}(\gamma k) = \hat{U}(k)\exp\left[-\delta^2\frac{\tan\theta}{2}k^3\mathcal{L}\right], \tag{4.4}$$

where $\mathcal{L} = L_a/\lambda_0$ is the non-dimensional length of the wave attractor. We consider $L_a \gg \lambda_0$, such that the discussed asymmetry of the attractor is negligible. As a consequence, the attenuation rate $-\delta^2(\tan\theta/2)k^3\mathcal{L}$ per attractor cycle can be orders of magnitude larger than $O(\delta^2k^3)$, namely if $\mathcal{L} \gtrsim \delta^{-1} \gg 1$ (note that by assumption, the most energetic wavenumber is non-dimensionalized to 2π).

The spectral constraint (4.4) for the velocity field is equivalent to the constraint for the buoyancy gradient spectrum, $A(k)$, given by Hazewinkel *et al.* (2008) upon correcting for a missing factor $1/2$ in their viscous attenuation rate, and a missing factor γ^{-1} on the right-hand side of their recursive relation $A_n^2 = \gamma^3 A_{n-1}^2$, where A_n and A_{n-1} are the buoyancy gradient spectra before and after the reflection from the slope, respectively.

The constraint (4.4) for $\hat{U}(k)$ now admits integrable finite-energy spectra:

$$\hat{U}(k) = P(\log_\gamma(k)) \exp\left[-\beta_1 k^3\right], \quad \text{with } \beta_1 = \frac{\delta^2 \mathcal{L} \tan\theta}{2(\gamma^3 - 1)} \tag{4.5}$$

for continuous period-1 functions P. The function $P(\log_\gamma(k))$ in the spectral solution (4.5) still reflects the geometric wave focusing, which projects the internal wave field distribution on any wavenumber interval $[k,\ \gamma k]$ onto $[\gamma k,\ \gamma^2 k]$, whereas the exponential term accounts for the energy dissipation upon travelling once around the wave attractor. If the energy input occurs within a low wavenumber interval, say $I_* = [k_*,\ \gamma k_*]$, with distribution $E(k)$, then $P(m) = \sqrt{E(\exp[\log(\gamma)m])}$ defines $P(m)$ for all $m > \log_\gamma(k_*)$ (by periodic continuation) and we take $P(m) = 0$ for $m < \log_\gamma(k_*)$ (no energy at wavenumbers smaller than k_*). If the energy input is spread over a wider interval than I_*, then one can split it into several intervals, define corresponding functions P for each interval and superimpose the resulting spectra. For mathematical convenience, we take $P(m)$ to be periodic with period 1 in the following.

If the energy input is discrete, say occurring only at fixed wavenumber k_*, then the function P must have a spike at $\log_\gamma(k_*)$ (a Dirac delta function), and P thus consists of a superposition of Dirac delta functions by periodic continuation. The spectrum $\hat{U}(k)$ then peaks at wavenumbers $k_*\gamma^n$ for $n = 0,\ 1,\ 2,\ \ldots$. The (discrete) spectral model derived by Hazewinkel *et al.* (2008) corresponds to this special case. We also discuss this discrete case in the comparison section, § 7.

In the next section, we show that the dissipation at the lateral walls also adds an exponential attenuation factor to the spectral constraint (4.4).

5. Dissipation at lateral walls

In this section we extend the wave attractor velocity field to the lateral walls, $y = \pm l_y$, where we apply the no-slip boundary condition. Again, we do this for one (arbitrary) wave attractor branch with interior velocity field $\boldsymbol{u}_0 = \hat{\boldsymbol{\xi}} U$, and phase speed along $\hat{\boldsymbol{\zeta}}$. Using the stretched coordinate $\eta = \delta^{-1} y$, the momentum equations for u_0 and w_0 are given by

$$-\mathrm{i}u_0 = -p_{0_x} + u_{0_{\eta\eta}}, \quad \mathrm{i}\cot^2\theta w_0 = -p_{0_z} + w_{0_{\eta\eta}}. \tag{5.1a,b}$$

In these two equations, the partial time derivatives have already been replaced by $-\mathrm{i}$. It is the buoyancy, $b_0 = -\mathrm{i}\sin^{-2}\theta\ w_0$, which adds to the time derivative of the vertical velocity component, w_0, producing the factor $-\cot^2\theta$. Outside the boundary layers, the along-wave-beam velocity component U is related to the pressure gradient in ζ-direction by

$$-\mathrm{i}\hat{\xi}_x U = -\hat{\zeta}_x p_{0_\zeta} \quad \Rightarrow \quad p_{0_\zeta} = -\mathrm{i}\cot\theta U, \tag{5.2}$$

which solves the momentum equations in the unstretched coordinates at $O(\delta^0)$, i.e. (5.1) without the diffusive terms. Here, $\hat{\xi}_x = \pm\cos\theta$ is the x-component of the unit vector $\hat{\boldsymbol{\xi}}$, and similarly $\hat{\zeta}_x = \pm\sin\theta$, the sign again depending on the branch. Solving (5.1) with no-slip boundary conditions at the walls, $\eta = \pm\delta^{-1} l_y$, and interior velocity field $\hat{\boldsymbol{\xi}} U$ in the centre plane, $\eta = 0$, gives

$$u_0 = \hat{\xi}_x \left(1 - \frac{\cosh[\mathrm{i}^{-1/2}\eta]}{\cosh[\mathrm{i}^{-1/2}\delta^{-1} l_y]}\right) U, \quad w_0 = \hat{\xi}_z \left(1 - \frac{\cosh[\mathrm{i}^{1/2}\cot\theta\,\eta]}{\cosh[\mathrm{i}^{1/2}\cot\theta\,\delta^{-1} l_y]}\right) U. \tag{5.3a,b}$$

The presence of stratification (non-zero buoyancy) causes the factor-$\cot\theta$ difference in the thicknesses of the boundary layer, δ and $\delta\tan\theta$, for respectively horizontal and vertical velocity components, making $(u_0, 0, w_0)$ divergent near the walls. This peculiar twist of the stratification on the boundary layer thickness was previously found by Vasiliev & Chashechkin (2003) in their theoretical study on 3-D internal wave generation by an inclined plane oscillating in the planar direction.

Note that the y-momentum equation is satisfied at $O(\delta)$ by choosing an appropriate pressure $p_2(\eta)$, which is $O(\delta^2)$, and thus negligible. By the continuity equation at $O(\delta^0)$ in stretched coordinate η,

$$u_{0_x} + w_{0_z} = -v_{1_\eta}, \tag{5.4}$$

we get the $O(\delta)$ transversal velocity component

$$v_1 = \cos\theta\sin\theta\left(\mathrm{i}^{1/2}\frac{\sinh[\mathrm{i}^{-1/2}\eta]}{\cosh[\mathrm{i}^{-1/2}\delta^{-1}l_y]} - \mathrm{i}^{-1/2}\tan\theta\frac{\sinh[\mathrm{i}^{1/2}\cot\theta\eta]}{\cosh[\mathrm{i}^{1/2}\cot\theta\delta^{-1}l_y]}\right)U_\zeta + V(y). \tag{5.5}$$

Here, $V(y)$ is an undetermined velocity component satisfying $V_\eta(y) \in O(\delta)$, that is to say, slowly varying in the transversal y-direction. The impermeability boundary condition ($v_1 = 0$) at both walls translates to

$$\left.\begin{gathered} V(\pm l_y) = \pm\sigma U_\zeta, \quad \text{with} \\ \sigma = \cos\theta\sin\theta(\mathrm{i}^{-1/2}\tan\theta\tanh[\mathrm{i}^{1/2}\cot\theta\delta^{-1}l_y] - \mathrm{i}^{1/2}\tanh[\mathrm{i}^{-1/2}\delta^{-1}l_y]). \end{gathered}\right\} \tag{5.6}$$

In the limit $\delta^{-1}l_y \gg 1$, the expression simplifies to $\sigma = -\mathrm{i}^{1/2}\sin\theta\mathrm{e}^{\mathrm{i}\theta}$. The transversal velocity component V enters the continuity equation at $O(\delta)$ in the unstretched coordinates:

$$U_\xi + \delta V_y = 0. \tag{5.7}$$

Since U is y-independent, we get $V_{yy} = 0$, hence

$$V = \frac{\sigma y}{l_y}U_\zeta. \tag{5.8}$$

Thus, the transversal velocity v decays linearly (hence slowly) towards the centre plane, $y = 0$, making the velocity field in the interior truly three-dimensional at $O(\delta l_y^{-1})$.

The transversal divergence,

$$V_y = \frac{\sigma}{l_y}U_\zeta = \frac{\mathrm{i}\sigma}{l_y}\int_0^\infty k\hat{U}(k)\exp\left[\mathrm{i}k\zeta - \mathrm{i}t\right]\mathrm{d}k, \tag{5.9}$$

is balanced by $-\delta^{-1}U_\xi$, according to the continuity equation (5.7). This means that U must be ξ-dependent at $O(\delta)$. For the velocity expressions (3.2) and (3.4) of the wave attractor, this requires the spectrum $\hat{U}(k)$ to be replaced by $\hat{U}(k)\exp\left[-\mathrm{i}\delta l_y^{-1}\sigma k\xi\right]$. Consequently, the velocity U decays in the along-wave-beam direction, ξ, with $\exp[-\delta l_y^{-1}\sigma_0 k\xi]$, where $\sigma_0 = \mathrm{Re}[\mathrm{i}\sigma] > 0$ for $\theta \in (0, \pi/2)$. The imaginary part of $\mathrm{i}l_y^{-1}\sigma$, which takes both positive and negative values for $\theta \in (0, \pi/2)$, describes a slight change in tilt in phase propagation direction, that changes from ζ to $\zeta - \delta l_y^{-1}\mathrm{Re}[\sigma]\xi$.

Adding the damping by the lateral walls to the constraint for the 2-D viscous wave attractor spectrum, (4.4), gives

$$\hat{U}(\gamma k) = \hat{U}(k) \exp\left[\left(-\delta^2 \frac{\tan\theta}{2} k^3 - \mathrm{i}\delta \frac{\sigma}{l_y} k\right) \mathcal{L}\right]. \tag{5.10}$$

This extended equilibrium wave attractor spectrum constraint is solved by

$$\hat{U}(k) = P(\log_\gamma(k)) \exp\left[-\beta_1 k^3 - \beta_2 k\right], \quad \text{with } \beta_2 = \frac{\mathrm{i}\delta\mathcal{L}\sigma}{l_y(\gamma - 1)}, \tag{5.11}$$

for all period-1 functions P.

6. Dissipation at reflecting walls

No-slip reflection of 2-D monochromatic internal waves from a wall has been analysed theoretically for wave beams by Kistovich & Chashechkin (1995*a*,*b*). Whereas dissipation due to internal shear is included in the analysis by Kistovich & Chashechkin (1995*a*,*b*), they do not account for the energy loss in the viscous boundary layer, which also weakens the reflected wave beam. We are interested in precisely this energy loss at the reflecting wall, such that we can tell when it is negligible.

To begin with, we consider the inviscid free-slip velocity field at the inclined wall, $z = (l_x - x)\tan\alpha$, as this is the most general prescription of a planar reflecting boundary. Expressed in the rotated and shifted coordinate system of the inclined wall,

$$\begin{bmatrix} x' \\ z' \end{bmatrix} = \begin{bmatrix} \cos\alpha & -\sin\alpha \\ \sin\alpha & \cos\alpha \end{bmatrix} \cdot \begin{bmatrix} x - x_1 \\ z - z_1 \end{bmatrix}, \tag{6.1}$$

with z' normal to the wall (see sketch in figure 2), the inviscid free-slip velocity field at the inclined wall, $z' = 0$, is given by

$$\boldsymbol{u}_0^{[1]} + \boldsymbol{u}_0^{[4]} = \hat{\boldsymbol{x}}' \tilde{U}(x'), \quad \tilde{U}(x') = \frac{-\sin 2\theta}{\sin[\alpha - \theta]} \int_0^\infty \hat{U}(k) \exp\left[\mathrm{i}k \sin[\alpha + \theta] x' - \mathrm{i}t\right] \mathrm{d}k, \tag{6.2}$$

where we have used the velocity expressions from § 3 and the inviscid spectral constraint (3.10).

The task is now to find a quasi-2-D correction velocity field, $\tilde{\boldsymbol{u}} = [\tilde{u},\ 0,\ \tilde{w}]$, such that it annihilates the free-slip velocity (6.2) at the inclined wall, $z' = 0$, and decays exponentially towards the interior. Using the stretched coordinate $Z = \delta^{-1} z'$, the x'-momentum equation at $O(\delta^0)$, governing the velocity component $\tilde{u}_0' = \tilde{u}_0 \cos\alpha - \tilde{w}_0 \sin\alpha$ in the direction along the inclined wall, becomes

$$\mathrm{i}\left(\frac{\sin^2\alpha}{\sin^2\theta} - 1\right) \tilde{u}_0' = \tilde{u}_{0_{ZZ}}'. \tag{6.3}$$

As previously in (5.1), we have replaced the partial time derivatives with $-\mathrm{i}$, and used $\tilde{b}_0 = \mathrm{i}(\sin\alpha/\sin^2\theta)\tilde{u}_0'$. The pressure gradient is absent because the pressure is not modified by the no-slip boundary. Solving (6.3) for $\tilde{\boldsymbol{u}}_0 = \hat{\boldsymbol{x}}'\tilde{u}_0'$ such that it annihilates (6.2) at $z' = Z = 0$ and vanishes in the interior, $Z' \to -\infty$, gives

$$\tilde{\boldsymbol{u}}_0 = -\hat{\boldsymbol{x}}' \tilde{U}(x') \exp\left[\mathrm{i}^{1/2} \mu Z\right] \quad \text{with } \mu = \sqrt{\frac{\sin^2\alpha}{\sin^2\theta} - 1}. \tag{6.4}$$

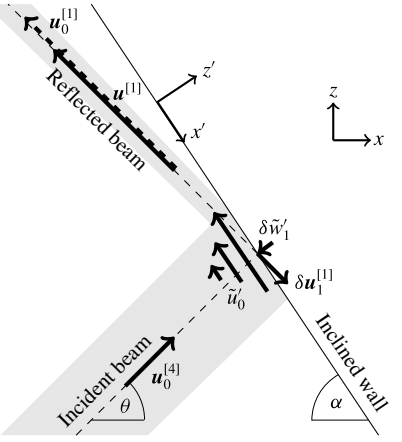

FIGURE 2. This sketch illustrates the velocity components involved in the reflection of the wave attractor (dashed line, wave motion confined to shaded area) at the inclined wall (solid line), with arrows pointing in the energy propagation directions. The velocity field of the reflected beam, $\boldsymbol{u}^{[1]} = \boldsymbol{u}_0^{[1]} + \delta\boldsymbol{u}_1^{[1]} + O(\delta^2)$, is – due to focusing – larger in amplitude than the incident beam velocity, $\boldsymbol{u}_0^{[4]}$, but weaker than the free-slip reflected velocity field, $\boldsymbol{u}_0^{[1]}$ (dashed arrow). The velocity component $\tilde{u}_0'$, pointing along the wall, annihilates the free-slip velocity field $\boldsymbol{u}_0^{[1]} + \boldsymbol{u}_0^{[4]}$ at the wall, $z' = 0$, and decays exponentially towards the interior. By mass conservation, it generates the velocity component $\tilde{w}_1'$ at $O(\delta)$, normal to the wall, which itself is cancelled by $\hat{\boldsymbol{z}}'\boldsymbol{u}_1^{[1]}$ at $z' = 0$. Contrary to $\tilde{u}_0$ and $\tilde{w}_1$, the component $\boldsymbol{u}_1^{[1]}$ does not decay towards the interior; it is the correction on the reflected beam due to damping by the no-slip reflection.

By the continuity equation at $O(\delta^0)$ in stretched coordinate Z,

$$\tilde{u}_{0_{x'}}' + \tilde{w}_{1_Z}' = 0, \tag{6.5}$$

with $\tilde{w}_1'$ the $O(\delta)$-velocity component normal to the wall, we get

$$\tilde{w}_1' = i^{-1/2}\mu^{-1}\tilde{U}_{x'}(x')\exp\left[\mathrm{i}^{1/2}\mu Z\right] + F(x', z'). \tag{6.6}$$

Here, F is an undetermined velocity component, with spatial variations of $O(1)$, similar to V in the previous section. Previously, we were able to find a linear function in y for V, such that the impermeability boundary conditions at opposite lateral walls are satisfied. This procedure fails here (because there is no opposite inclined wall), and we must take $F = 0$. As a consequence, $\tilde{w}_1'$ describes an apparent flow through the inclined wall, $z' = Z = 0$. This apparent flow through the wall,

$$\tilde{w}_1'(x', Z = 0) = -\mathrm{i}^{1/2}\frac{\gamma\,\sin 2\theta}{\mu}\int_0^\infty k\hat{U}(k)\exp\left[\mathrm{i}k\sin[\alpha+\theta]x' - \mathrm{i}t\right]\,\mathrm{d}k, \tag{6.7}$$

can be balanced by absorbing some $O(\delta)$-fraction of the incident wave beam (see also illustration in figure 2). Consequently, the viscously reflected beam with velocity field $\boldsymbol{u}^{[1]} = \boldsymbol{u}_0^{[1]} + \delta\boldsymbol{u}_1^{[1]} + O(\delta^2)$ is weaker than the inviscid velocity field, $\boldsymbol{u}_0^{[1]}$. We write

$$\boldsymbol{u}^{[1]} = \hat{\xi}_1\int_0^\infty \hat{U}(k)\exp[-\delta R_\alpha k]\exp\left[\mathrm{i}k\zeta_1 - \mathrm{i}t\right]\,\mathrm{d}k, \tag{6.8}$$

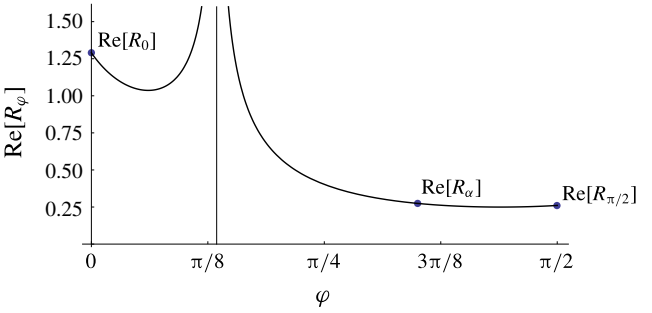

FIGURE 3. This figure presents the $O(\delta)$-dissipation rate, $\mathrm{Re}[R_\varphi]$, as a function of the angle φ of the reflecting wall with respect to the vertical, for $\theta = 0.42$ rad. As to be expected, R_φ blows up at the critical reflection angle, $\varphi = \theta = 0.42$ (vertical asymptote). The total dissipation by no-slip reflections of a wave attractor such as in figure 1(*a*) is the sum of dissipation rates at the bottom ($\mathrm{Re}[R_0]$), the inclined wall ($\mathrm{Re}[R_\alpha]$, here $\alpha = 1.1$) and the vertical wall ($\mathrm{Re}[R_{\pi/2}]$).

such that

$$\boldsymbol{u}_1^{[1]} = -\hat{\xi}_1 R_\alpha \int_0^\infty k\hat{U}(k)\exp\left[\mathrm{i}k\zeta_1 - \mathrm{i}t\right]\,\mathrm{d}k, \tag{6.9}$$

where $\delta\mathrm{Re}[R_\alpha] > 0$ is the dissipation rate (per wavenumber) due to the reflection.

The complex-valued reflection dissipation rate R_α is determined by the impermeability condition at $O(\delta)$:

$$\tilde{w}_1' + \boldsymbol{u}_1^{[1]} \cdot \hat{\boldsymbol{z}}' = 0 \quad \text{at } z' = 0. \tag{6.10}$$

Substituting (6.7) and (6.9) into (6.10) and noting that on the inclined wall, $z' = 0$, we have $\zeta_1 = \sin[\alpha - \theta]x'$, gives

$$R_\alpha = \mathrm{i}^{1/2}\frac{\sin 2\theta}{\mu\,\sin[\alpha - \theta]}. \tag{6.11}$$

We can readily use expression (6.11) to determine the dissipation rates due to the reflections at respectively the flat bottom ($\alpha \to 0$) and the vertical wall ($\alpha \to \pi/2$):

$$R_0 = \mathrm{i}^{-1/2}2\cos\theta \quad \text{and} \quad R_{\pi/2} = \mathrm{i}^{1/2}2\sin\theta\tan\theta = \mathrm{i}\tan^2\theta R_0.f \tag{6.12a,b}$$

The dissipation rate (real part of (6.11)) as a function of the angle of the reflecting boundary is shown in figure 3. In laboratory and numerical set-ups, the surface of the fluid, $z = h$, is typically free, so the most appropriate constraint on this boundary is free slip (because vertical variations are negligibly small), i.e. no dissipation by reflection. The full viscous 3-D equilibrium wave attractor spectrum must thus satisfy

$$\hat{U}(\gamma k) = \hat{U}(k)\exp\left[-\delta^2\left(\mathcal{L}/2\tan\theta\right)k^3 - \delta\left(\mathrm{i}\sigma l_y^{-1}\mathcal{L} + R_\alpha + R_0 + R_{\pi/2}\right)k\right]. \tag{6.13}$$

Solutions to this spectral constraint are given by

$$\hat{U}(k) = P(\log_\gamma(k))\exp\left[-\beta_1 k^3 - \beta_2 k - \beta_3 k\right], \quad \text{with } \beta_3 = \delta\frac{R_\alpha + R_0 + R_{\pi/2}}{\gamma - 1}, \tag{6.14}$$

for arbitrary period-1 functions P. If not stated otherwise we always consider $P =$ constant in the following.

Brunt-Väisälä frequency	N_0	3	rad s^{-1}
Angle of wave beam with respect to horizontal	$\theta = \arcsin[\omega_0/N_0]$	0.42	rad
Angle of sloping wall with respect to horizontal	α	1.10	rad
Width of the tank	$W = 2l_y\lambda_0$	10.1	cm
Tank length at bottom	$L = 2l_x\lambda_0$	45.3	cm
Water column height	$H = h\lambda_0$	19.0	cm
Wave attractor length	$L_a = \mathcal{L}\lambda_0$	85.0	cm

TABLE 1. Parameter values of the laboratory experiment by Hazewinkel *et al.* (2008).

7. Comparison with laboratory experiments and 3-D simulations

We validate our theoretical results by comparing it with experimental spectral results by Hazewinkel *et al.* (2008) and Brouzet (2016) in §§ 7.1 and 7.2 respectively. Section 7.2 also includes a comparison with fully 3-D numerical simulations, replicating one of the experiments by Brouzet (2016).

7.1. *Comparison with laboratory experiment by Hazewinkel et al. (2008)*

Hazewinkel *et al.* (2008) studied the equilibrium spectrum of internal wave attractors in the classical trapezoidal set-up, both in the laboratory and with a simple model. The parameter values relevant for the comparison with our theory are listed in table 1. Using synthetic schlieren techniques, they directly measured the buoyancy gradient field, $[b_x, b_z]$. Spatial variations of this buoyancy gradient field for each wave attractor branch are primarily in the corresponding phase propagation directions, ζ. Figure 4 reproduces the normalized modulus of the observed spectrum $\hat{A}(k) = (-\mathrm{i}/\sin\theta)k\hat{U}(k)$ of the buoyancy gradient, b_ζ, pointing in the phase propagation direction of the first wave attractor branch, along transect S_1 as shown in figure 1(*a*) in Hazewinkel *et al.* (2008). For comparison, figure 4 shows our theoretical 3-D wave attractor spectrum (thick blue solid line) for different period-1 functions P in (6.14). Additionally, we present the theoretical 2-D spectrum including internal shear dissipation only ((4.5), dashed line in figure 4), which corresponds to the 2-D theoretical spectrum by Hazewinkel *et al.* (2008), their (4.6), for $P =$ constant and upon correcting mathematical mistakes in their analysis, mentioned in § 4. Note that Hazewinkel *et al.* (2008) seemingly achieved a good fit in their figure 6 because they changed their input wavenumber, $k_{in} = 2\pi/H$ (in their notation k_0), while keeping the same k_{in} fixed in their (4.6). Correct application of their theory reveals that their theoretical spectrum does not depend on their input wavenumber, k_{in}, and that the theoretical 2-D spectrum predicts the attractor wavelength to be a factor 2 smaller than observed. The mismatch between the 2-D spectra and observation supports our striking and unexpected conclusion that dissipation at the rigid walls must be substantial.

To illustrate the importance of the different dissipation mechanisms, we also present in figure 4 the spectra excluding dissipation upon reflection ((5.11), dotted blue line) and excluding internal shear dissipation ((6.14) with $\beta_1 = 0$, black dashed-dotted line) for $P =$ constant.

Three conclusions can be directly inferred from the comparison in figure 4.

(i) The full 3-D wave attractor spectrum fits the observed spectrum reasonably well for the choices $P =$ constant and $P(k) = P_c(k) = 3 + \cos(2\pi k)$. The contact surface of the wave attractor with the tank boundaries (shaded surfaces in figure 1*a*)

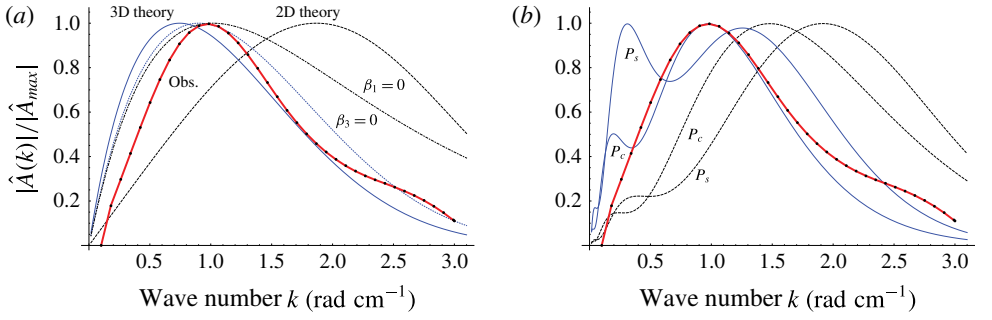

FIGURE 4. (Colour online) Normalized modulus of the buoyancy gradient spectra, $\hat{A}(k) \propto k\hat{U}(k)$. The red curves with black dots reproduce the observed spectrum by Hazewinkel *et al.* (2008). Theoretical spectra are presented in plot (*a*) with $P =$ constant and in plot (*b*) with $P_s(k) = 3 + \sin(2\pi k)$, $P_c(k) = 3 + \cos(2\pi k)$: 3-D spectrum ((6.14), thick blue) and 2-D spectrum ((4.5), black dashed). Panel (*a*) also shows the spectra excluding dissipation upon reflection ((5.11), i.e. $\beta_3 = 0$, dotted blue) and excluding internal shear dissipation ((6.14) with $\beta_1 = 0$, black dashed-dotted).

consists primarily (∼73 %) of those at the lateral walls. It thus comes as no surprise that in this particular laboratory set-up, with $\beta_3 \approx 0.28\beta_2$, neglecting dissipation at the reflecting walls still results in good fits with the observation (see also relatively small difference between solid and dotted blue lines in figure 4*a*). Hence, dissipation occurs primarily in the internal shear layers and in the lateral boundary layers, and secondarily also at the reflecting rigid boundaries.

(ii) Neglecting internal shear dissipation ((6.14) with $\beta_1 = 0$, dashed-dotted line) leads to a spectrum whose peak coincides with the observation. However, at large wavenumbers, this spectrum diverges from the observation. This indicates that the neglected internal shear dissipation, which is cubic in wavenumber k, is the dominant dissipation mechanism at high wavenumbers in the laboratory experiment.

(iii) The discrepancy between the full 3-D spectrum for $P_c(k) = 3 + \cos(2\pi k)$ and $P_s(k) = 3 + \sin(2\pi k)$ shows that the shape of the theoretical spectrum depends strongly on this period-1 function, P. As discussed in § 4, the precise nature of the P is set by the spatial structure of the energy input, i.e. by the geometry of the tank used in the experiment by Hazewinkel *et al.* (2008). This means that the energy input strongly influences the spatial structure of the equilibrium wave attractor, and upscaling of a laboratory set-up generally does not leave the wave attractor invariant. Despite the sensitivity on P, we can only achieve reasonable fits between theory and observations if we include dissipation at the rigid boundaries, which is dominated by lateral walls dissipation.

7.2. *Comparison with laboratory experiments by Brouzet (2016) and 3-D simulation*

Following Scolan *et al.* (2013), Brouzet (2016) performed laboratory experiments on wave attractors in a trapezoidal tank using a wave generator. They especially carried out experiments in two trapezoidal tanks with almost identical lateral width (W), but with differences in height (H) and attractor length (L_a) of approximately a factor 3 (see table 2 for parameter values). Here, we briefly describe the experiments for a comparison with our theory

		Small tank	Large tank	
Brunt–Väisälä frequency	N_0	1.37	0.867	rad s^{-1}
Angle of wave beam with respect to the horizontal	$\theta = \arcsin[\omega_0/N_0]$	0.61	0.58	rad
Angle of sloping wall with respect to the horizontal	α	1.13	1.18	rad
Width of the tank	$W = 2l_y\lambda_0$	17.0	17.4	cm
Water column height	$H = h\lambda_0$	29.5	92.0	cm
Wave attractor length	$L_a = \mathcal{L}\lambda_0$	103.3	337.8	cm
Wave maker amplitude	a	2.5	1.5	mm

TABLE 2. Parameter values of the laboratory experiments by Brouzet (2016).

In both experimental set-ups, the internal waves are generated by a sinusoidally shaped wave maker (Gostiaux *et al.* 2007) situated on the left side of the tank, with the vertical wavelength corresponding to half the height of the water column, so $k_{in} = \pi/H\cos\theta$. Previous experiments (Scolan *et al.* 2013), also reported in Brouzet *et al.* (2016*a*,*b*, 2017*a*), show that triadic resonance instabilities arise if the wave maker amplitude, a, exceeds a critical values in the range 2.5–3 mm, dependent on the position of the attractor. Both experiments presented here are stable, and a steady state is reached after a spin-up of approximately 20 wave periods.

Figure 5(*a*,*b*) presents two snapshots of the observed buoyancy gradient field, b_ζ, in steady state, with the derivative taken in the phase propagation direction of the first branch. The Fourier spectra along the depicted transects are shown in figure 5(*c*,*d*). (The experimental non-dimensional buoyancy gradient $b_\zeta = g/(\rho_0 N_0^2)\rho'_\zeta$, where $\rho_0 = 1000$ kg m^{-3} the background density, g gravitational acceleration, coordinate ζ now understood dimensional, and ρ' the density perturbation, is first projected onto 1000 data points along each depicted transect; then it is Fourier transformed using Fast Fourier transform in MATLAB with zero padding to get 10 000 data points in Fourier space.) For comparison, figure 5(*c*,*d*) also present the theoretical spectra with and without rigid-wall dissipation for $P =$ constant (solid and dashed lines, respectively). Figure 5(*d*) also includes the spectrum of the numerical simulation (simulation output is directly saved on an inclined (ζ, y)-plane (40×173 grid-points), which intersects the first wave attractor branch at the dot-dashed transect in figure 5(*b*). The simulated density perturbation is differentiated with respect to ζ, averaged in the y-direction (excluding 10 grid points in lateral boundary layer) and ω_0-Hilbert filtered over the last 63 wave periods of the simulation (simulation lasted 107 wave periods), before computing the spectrum (with zero padding to get 120 data points in Fourier space).) for the large tank set-up, discussed below.

The dots on the solid blue line of the fully dissipative spectra indicate the hypothetical spikes of $\hat{U}(k)$ at $k = \gamma^n k_{in}$, $n = 0, 1, 2, \ldots$, which occur according to our theory if the energy is confined to precisely k_{in}. Such spikes are by no means visible in the experimental and simulated spectra. We believe that due to imperfections in the laboratory set-up and numerics in the simulation, the experimental and simulated energy inputs do not occur precisely at k_{in}, but over a continuous range of wavenumbers near k_{in}. The spectra with $P =$ constant capture such continuous energy input over a range of wavenumbers. We have no reason to believe that $P =$ constant is the best representation of the actual energy input. Different period-1 functions P

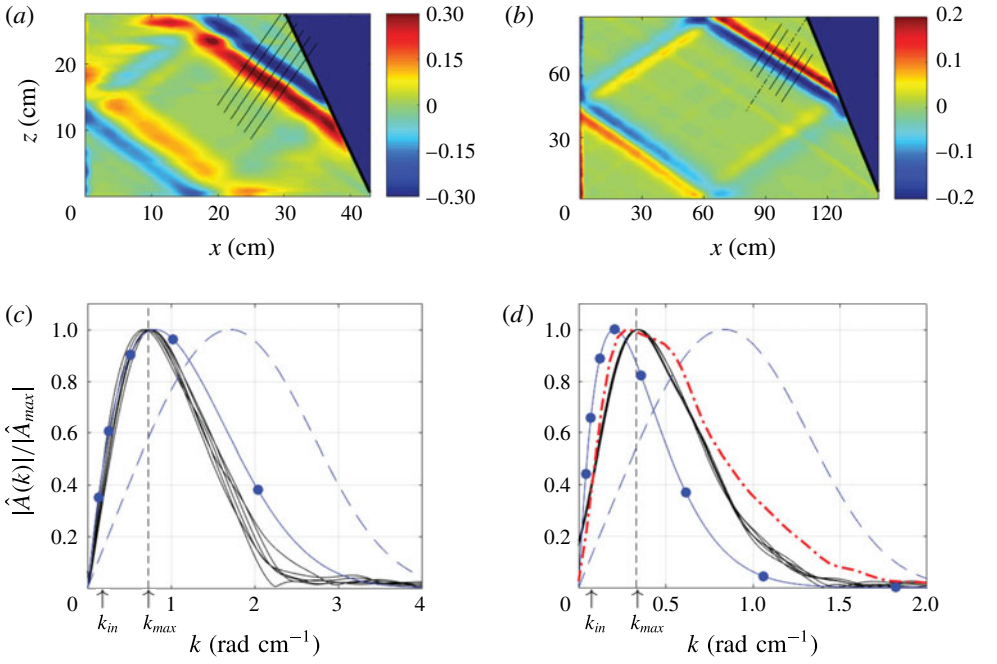

FIGURE 5. (Colour online) Experimental results by Brouzet (2016) in the small and large tank set-ups. (*a*,*b*) Snapshots of the buoyancy gradient, b_ζ, in the phase propagation direction ζ of first branch, derived from observed field $[b_x, b_z]$ after Hilbert filtering at ω_0. (*c*,*d*) Normalized modulus of experimental buoyancy gradient spectra, $|\hat{A}|/|\hat{A}_{max}|$, (black lines) along the depicted transects of the first attractor branch in (*a*,*b*). For comparison, corresponding 3-D theoretical spectra (solid blue) and 2-D spectra (dashed blue) for $P =$ constant; the blue dots indicate the discrete 3-D spectra with energy input only at k_{in}. The red dot-dashed curve in (*d*) shows the numerical spectrum taken along the dot-dashed transect in (*b*) after ω_0-Hilbert filtering simulated steady-state time series of the large tank set-up. See text for additional explanation.

(not shown) lead to similar discrepancies between 3-D theory and experimental spectra in figure 5(*d*).

Despite small discrepancies in figure 5(*d*), it is clear that for both experimental set-ups the correspondence between the observation and our 3-D model is best. This supports our new conclusion that dissipation at the rigid walls (mostly at the lateral walls) is significant even for very small ratios of boundary layer thickness over lateral width, $d_0/W \sim O(10^{-2})$.

Fully 3-D simulations are run for the 'large tank' set-up (see table 2) with the method of spectral elements, which combines the accuracy and high resolution of spectral methods with geometric flexibility of finite element methods (see Brouzet *et al.* (2016*b*), Sibgatullin & Kalugin (2016) for details on the numerical method). Figure 6 presents two snapshots of the steady-state buoyancy field in a $\xi =$ constant plane (dot-dashed transect in figure 5*d*), intersecting the first wave attractor branch in the phase-propagating direction, ζ. We present only $\sim$6 % of the transversal wall-to-wall distance, to magnify the boundary layer structure near the lateral wall (here at $y = 0$). For comparison, we show the theoretical buoyancy field for spectra with and without rigid-wall dissipation. The theoretical buoyancy field for the fully

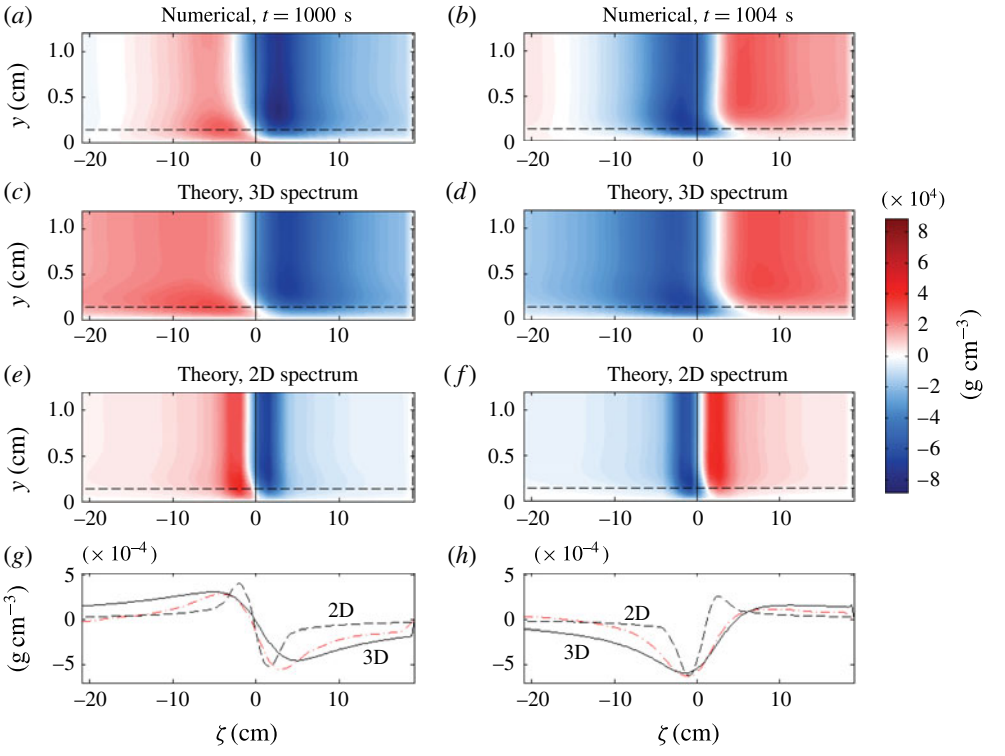

FIGURE 6. (Colour online) Snapshots (*a–f*) of the density perturbation (= proportional to buoyancy b) in an inclined plane, $\xi =$ constant, along the phase propagation direction ζ (dot-dashed transect in figure 5*b*), and in the vicinity of one lateral wall (here $y = 0$). Simulated density perturbation at times $t = 1000$ s (*a*), and 0.3 wave periods later, at $t =$ 1004 s (*b*), are plotted on top of corresponding theoretical density perturbation for the fully dissipative attractor (3-D spectrum, plots *c*,*d*) and for internal shear dissipation only (2-D spectrum, plots *e*,*f*). The (buoyancy) boundary layer widths, $d_0 \tan\theta = 0.13$ cm and $d_0\mu$ at respectively lateral wall ($y = 0$) and inclined wall ($\zeta = 19$ cm), are indicated by the dashed lines; the solid line shows the centre of the wave attractor. In (*g*) and (*h*) comparison of simulated (dot-dashed red) and theoretical (3-D in solid, 2-D in dashed) density perturbations in the panels above along $y = d_0 \tan\theta = 0.13$ cm (dashed in above graphs).

dissipative spectra (middle panels, maximum amplitude scaled to maximum amplitude of simulation) agrees with the numerical simulation remarkably well. In contrast, neglecting rigid-wall dissipation leads to a much thinner wave attractor, which might even be unstable to triadic resonance instabilities for this experiment.

Figure 6 also visualizes the complex structure of the buoyancy field in the lateral boundary layer, which is of relevance to secondary processes, such as mean flow generation. In fact, we find that the transversal velocity component, v, (not shown) is dominated by a mean component. Our linear theory cannot capture the induced mean flow, discussed in §4.4 of Brouzet (2016), which increases continuously throughout the simulated 107 wave periods.

Last but not least: the comparison of buoyancy gradient spectra in figure 5(*d*) shows that simulated and experimentally observed spectral properties agree very well, thereby confirming that wall dissipation is also important for the numerical simulation.

Our results suggests that similar 2-D simulations by Grisouard *et al.* (2008), meant to replicate quasi-2-D laboratory set-ups, probably miss significant dissipation at the lateral walls. We speculate that the lateral wall dissipation shifts the onset of triadic resonance instabilities towards stronger energy input, i.e. larger wave attractor amplitude a in the experiments by Scolan *et al.* (2013) and Brouzet (2016).

7.3. *Scaling of wave attractors*

There is an ongoing debate on the scaling of wave attractors (Rieutord *et al.* 2001; Ogilvie 2005; Grisouard *et al.* 2008; Hazewinkel *et al.* 2008; Brouzet 2016; Brouzet *et al.* 2017*b*). Our new analysis predicts that the scaling of wave attractors depends on the type of energy dissipation. We define the characteristic wavelength of the attractor as $2\pi/k_{max}$, where k_{max} is the dimensional wavenumber corresponding to the maximum of the spectrum. Considering only internal shear dissipation ((4.5) with $P=$ constant), we get the characteristic attractor wavelength $\lambda_0^I = 2\pi/k_{max} = 2\pi\ (3\beta_1)^{1/3}$, where β_1 is now understood as the dimensional equivalent of its non-dimensional definition in (4.5), taking d_0 instead of δ, and L_a instead of $\mathcal{L}$. We recover $\lambda_0^I \propto (L_a\nu/N_0)^{1/3}$, as originally found by Rieutord *et al.* (2001) and numerically verified by Grisouard *et al.* (2008). Damping only by the lateral walls ((5.11) with $\beta_1 = 0$) results in an attractor wavelength $\lambda_0^W = 2\pi\mathrm{Re}[\beta_2] \propto (L_a/W)\ (\nu/N_0)^{1/2}$, with β_2 also understood to be dimensional. Interestingly, this attractor length scale, λ_0^W, is independent of the actual size of the 3-D tank, because scaling both L_a and W leaves λ_0^W invariant. The dissipation at the lateral walls is negligible only if $\lambda_0^I \gg \lambda_0^W$, which is the case when

$$W \gg L_a^{2/3} d_0^{1/3} \sigma_0 \frac{[\cot\theta\ \ 2(\gamma^3-1)/3]^{1/3}}{2(\gamma-1)}. \tag{7.1}$$

Figure 7 shows λ_0 as a function of L_a for the parameter values of the small and large tank set-ups by Brouzet (2016), with the dots showing the experimentally observed characteristic wavelengths (corresponding to k_{max} indicated in figure 5*c*,*d*). The two graphs do not coincide due to slightly different parameter values, most prominently differences in angle α for the two set-ups. One can distinguish two different regimes: (i) For $L_a \gg W$, lateral wall dissipation dominates, so $\lambda_0^W \propto L_a$. (ii) For $W \lesssim L_a$, internal shear dissipation contributes significantly, so $\lambda_0^I \propto L_a^{1/3}$. The presented experiments fall into the transition between region (i) and (ii). This stresses the importance of previously unrecognized dissipation at rigid lateral walls.

8. Concluding remarks

From our theoretical analysis it is evident that the structure of a wave attractor in equilibrium is primarily determined by wave focusing, viscous dissipation at the rigid boundaries (mostly at the lateral walls), as well as viscous dissipation in the internal shear layers. Contrary to what was previously suggested, we show that the quasi-2-D experiments by Hazewinkel *et al.* (2008) cannot be captured by the theoretical spectrum of a 2-D steady-state wave attractor, which takes only internal shear dissipation into account. We close the gap between observations and theory by adding viscous dissipation at the lateral walls, which are the primary contact surfaces of the attractor and the rigid boundaries in the experiment by Hazewinkel *et al.* (2008). It is clear that rigid-wall dissipation also plays an important role in the experiments by Scolan *et al.* (2013) and Brouzet (2016).

Contrary to previous studies, we find that the shape of the equilibrium wave attractor in the classical trapezoidal set-up is not only dependent on the properties of

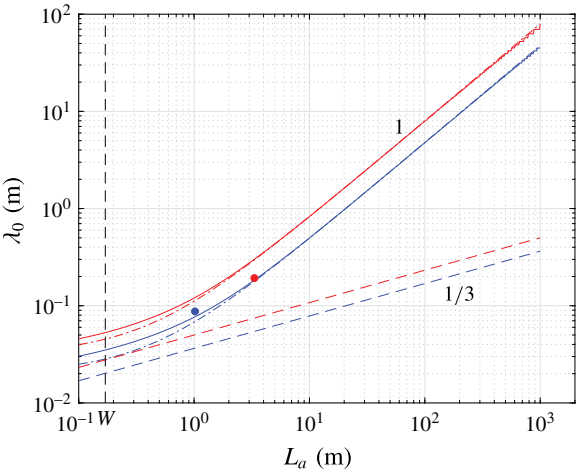

FIGURE 7. (Colour online) Theoretical wavelength λ_0, as function of orbital attractor length, L_a, for parameter values corresponding to 'small tank' (blue) and 'large tank' (red), with the dots showing the observed wavelength at the actual orbital lengths (1 m and 3 m, respectively). Solid lines: scaling of λ_0 as a function of L_a for fixed W and fully dissipative attractor (value $W = 0.17$ m is marked). Dashed lines: scaling for internal shear damping only ($\lambda_0^I \propto L_a^{1/3}$). Dot-dashed lines: rigid-wall dissipation only ($\lambda_0^W \propto L_a$).

the stratified fluid (viscosity ν, Brunt–Väisälä frequency N_0), the geometry of the tank (width W, wave attractor length L_a, sloping wall angle α) and forcing frequency ω_0, but also on the nature of the energy input, which determines the period-1 function P in (4.5), (5.11) and (6.14). Whereas the fluid properties and geometry determine the characteristic cross-beam wavelength of the wave attractor, the nature of the energy input sets the fine structure of the equilibrium wave attractor. The role of the period-1 function P remains vague, and more research is needed to understand the relation between a single wavenumber energy input and a continuous steady-state wave attractor spectrum.

The striking unresolved problem is the following: if the energy input is discrete, as one may argue for the 'small tank' and 'large tank' set-ups, then the period-1 function P should consist of Dirac delta functions, leading to a discrete spectrum. However, the experimental and simulated spectra with supposedly discrete energy input are smooth. It is unclear whether the energy input is not as discrete in spectral space as we imagined, or whether some other mechanism (not captured by our theory) effectively smooths the wave attractor spectrum.

In the ocean, sites where internal waves propagate parallel to a rigid vertical boundary over long distances are sparse; the channel between two coral atolls studied by Rayson *et al.* (2016) being such exceptional example. Wave beam reflection at bottom topography is much more common. To the best of our knowledge, we are the first to explicitly determine the dissipation due to such reflection. Our assumption of a stable laminar boundary layer holds in the ocean for semi-diurnal tides with amplitudes up to 32 m (Bukreev 1988). For internal tides with wavelengths of the order of 100 m ($k_0 = 0.06$ rad m^{-1}), we find that the velocity amplitude decay due to non-critical reflection, $d_0 k_0 R_\alpha$, can amount up to $\sim 1\,\%$. For larger wavelengths, the decay is even smaller, confirming that dissipation due to laminar reflection is typically negligible in the ocean. Probably more important is the three-dimensionality

of the boundary layer velocity field occurring for reflecting wave beams, which happens if incoming and outgoing beams point in different horizontal directions. It is well known that the 2-D steady-state similarity linear solutions for collinear viscous wave beams by Tabaei & Akylas (2003) can also be valid in the nonlinear regime. This may change in the vicinity of the rigid boundary, where Reynolds stresses may become large. Consequences can be the generation of strong mean flows, such as observed experimentally by Bordes *et al.* (2012) and Grisouard *et al.* (2013), and in the simulations by King, Zhang & Swinney (2010) and by K. Raja (personal communication), or triadic resonance instability (Scolan *et al.* 2013; Brouzet *et al.* 2016*a*, 2017*a*). Both scenarios may result in the breakdown of the internal wave beam, strong energy dissipation near the reflecting boundary and potentially vertical mixing (Dauxois *et al.* 2018).

Acknowledgements

We thank T. Dauxois, E. Ermanyuk, J. Frank, S. Joubaud and K. Raja for helpful discussions, and three anonymous reviewers for their input leading to an improved manuscript. I.N.S. is partially supported by the Russian Foundation for Basic Research 15-01-06363, and the Russian Science Foundation 14-50-00095. The numerical simulations were performed on the supercomputer Lomonosov of Moscow State University. F.B. is grateful for support by NWO Mathematics of Planet Earth grant 657.014.006.

REFERENCES

BECKEBANZE, F. & KEADY, G. 2016 On functional equations leading to exact solutions for standing internal waves. *Wave Motion* **60**, 181–195.

BECKEBANZE, F. & MAAS, L. R. M. 2016 Damping of 3d internal wave attractors by lateral walls. In *Proc. VIIIth Int. Symp. on Stratified Flows.* San Diego, 29 August–1 September 2016, pp. 1–6. University of California at San Diego.

BORDES, G., VENAILLE, A., JOUBAUD, S., ODIER, P. & DAUXOIS, T. 2012 Experimental observation of a strong mean flow induced by internal gravity waves. *Phys. Fluids* **24**, 086602.

BROUZET, C. 2016. Internal-wave attractors: from geometrical focusing to non-linear energy cascade and mixing. PhD thesis, ENS de Lyon.

BROUZET, C., ERMANYUK, E. V., JOUBAUD, S., PILLET, G. & DAUXOIS, T. 2017*a* Internal wave attractors: different scenarios of instability. *J. Fluid Mech.* **811**, 544–568.

BROUZET, C., ERMANYUK, E. V., JOUBAUD, S., SIBGATULLIN, I. & DAUXOIS, T. 2016*a* Energy cascade in internal wave attractors. *Europhys. Lett.* **113**, 44001.

BROUZET, C., SIBGATULLIN, I. N., ERMANYUK, E. V., JOUBAUD, S. & DAUXOIS, T. 2017*b* Scale effects in internal wave attractors. *Phys. Rev. Fluids* **2**, 114803.

BROUZET, C., SIBGATULLIN, I. N., SCOLAN, H., ERMANYUK, E. V. & DAUXOIS, T. 2016*b* Internal wave attractors examined using laboratory experiments and 3d numerical simulations. *J. Fluid Mech.* **793**, 109–131.

BUKREEV, I. V. 1988 Experimental investigation of the range of applicability of the solution of Stokes's second problem. *Fluid Dyn.* **23**, 504–509.

DAUXOIS, T., JOUBAUD, S., ODIER, P. & VENAILLE, A. 2018 Instabilities of internal gravity wave beams. *Annu. Rev. Fluid Mech.* **50**, 131–156.

DAUXOIS, T. & YOUNG, W. R. 1999 Near-critical reflection of internal waves. *J. Fluid Mech.* **390**, 271–295.

DINTRANS, B., RIEUTORD, M. & VALDETTARO, L. 1999 Gravito-inertial waves in a rotating stratified sphere or spherical shell. *J. Fluid Mech.* **398**, 271–297.

ECHEVERRI, P., YOKOSSI, T., BALMFORTH, N. J. & PEACOCK, T. 2011 Tidally generated internal-wave attractors between double ridges. *J. Fluid Mech.* **669**, 354–374.

GOSTIAUX, L., DIDELLE, H., MERCIER, S. & DAUXOIS, T. 2007 A novel internal waves generator. *Exp. Fluids* **42** (1), 123–130.

GRISOUARD, N., LECLAIR, M., GOSTIAUX, L. & STAQUET, C. 2013 Large scale energy transfer from an internal gravity wave reflecting on a simple slope. *Procedia IUTAM* **8**, 119–128.

GRISOUARD, N., STAQUET, C. & PAIRAUD, I. 2008 Numerical simulation of a two-dimensional internal wave attractor. *J. Fluid Mech.* **614**, 1–14.

GUO, Y. & HOLMES-CERFON, M. 2016 Internal wave attractors over random, small-amplitude topography. *J. Fluid Mech.* **787**, 148–174.

HARLANDER, U. 2008 Towards an analytical understanding of internal wave attractors. *Adv. Geosci.* **15**, 3–9.

HAZEWINKEL, J., VAN BREEVOORT, P., DALZIEL, S. B. & MAAS, L. R. M. 2008 Observations on the wave number spectrum and evolution of an internal wave attractor. *J. Fluid Mech.* **598**, 373–382.

HAZEWINKEL, J., MAAS, L. R. M. & DALZIEL, S. B. 2011 Tomographic reconstruction of internal wave patterns in a paraboloid. *Exp. Fluids* **50**, 247–258.

HAZEWINKEL, J., TSIMITRI, C., MAAS, L. R. M. & DALZIEL, S. B. 2010 Observations on the robustness of internal wave attractors to perturbations. *Phys. Fluids* **22** (10), 107102.

JOUVE, L. & OGILVIE, G. I. 2014 Direct numerical simulations of an inertial wave attractor in linear and nonlinear regimes. *J. Fluid Mech.* **745**, 223–250.

KING, B., ZHANG, H. P. & SWINNEY, H. L. 2010 Tidal flow over three dimensional topography generates out of forcing plane harmonics. *Geophys. Res. Lett.* **37**, 1–5.

KISTOVICH, Y. V. & CHASHECHKIN, Y. D. 1995*a* Reflection of packets of internal waves from a rigid plane in a viscous fluid. *Atmos. Ocean. Phys.* **30**, 718–724.

KISTOVICH, Y. V. & CHASHECHKIN, Y. D. 1995*b* The reflection of beams of internal gravity waves at a flat rigid surface. *Z. Angew. Math. Mech.* **59**, 579–585.

KLEIN, M., SEELIG, T., KURGANSKY, M. V., GHASEMI, V. A., BORCIA, I. D., WILL, A., SCHALLER, E., EGBERS, C. & HARLANDER, U. 2014 Inertial wave excitation and focusing in a liquid bounded by a frustum and a cylinder. *J. Fluid Mech.* **751**, 255–297.

LAMB, K. G. 2014 Internal wave breaking and dissipation mechanisms on the continental slope/shelf. *Annu. Rev. Fluid Mech.* **46**, 231–254.

MAAS, L. R. M. 2005 Wave attractors: linear yet nonlinear. *Intl J. Bifurcation Chaos* **15**, 2757–2782.

MAAS, L. R. M. 2009 Exact analytic self-similar solution of a wave attractor field. *Physica* D **238**, 502–505.

MAAS, L. R. M., BENIELLI, D., SOMMERIA, J. & LAM, F. P. A. 1997 Geometric focusing of internal waves. *Nature* **388**, 557–561.

MAAS, L. R. M. & LAM, F. P. A. 1995 Geometric focusing of internal waves. *J. Fluid Mech.* **300**, 1–41.

MANDERS, A. M. M. & MAAS, L. R. M. 2003 Observations of inertial waves in a rectangular basin with one sloping boundary. *J. Fluid Mech.* **493**, 59–88.

OGILVIE, G. I. 2005 Wave attractors and the asymptotic dissipation rate of tidal disturbances. *J. Fluid Mech.* **543**, 19–44.

RAYSON, M. D., BLUTEAU, C. E., IVEY, G. N. & JONES, N. L. 2016 Observations of high-frequency internal waves and strong turbulent mixing in a channel flow between two coral atolls. San Diego, 29 August-1 September 2016. In *Proc. VIIIth Int. Symp. on Stratified Flows*, University of California at San Diego.

RENAUD, A. & VENAILLE, A. 2018 Boundary streaming by internal waves. *J. Fluid Mech.* 1–10; (in press).

RIEUTORD, M., GEORGEOT, B. & VALDETTARO, L. 2001 Inertial waves in a rotating spherical shell: attractors and asymptotic spectrum. *J. Fluid Mech.* **435**, 103–144.

RIEUTORD, M., GEORGEOT, B. & VALDETTARO, L. 2002 Analysis of singular inertial modes in a spherical shell: the slender toroidal shell mode. *J. Fluid Mech.* **463**, 345–360.

SCHLICHTING, H. & GERSTEN, K. 2000 *Boundary-Layer Theory*. Springer.

SCOLAN, H., ERMANYUK, E. V. & DAUXOIS, T. 2013 Nonlinear fate of internal wave attractors. *Phys. Rev. Lett.* **110**, 234501.

SIBGATULLIN, I. & KALUGIN, M. 2016 High-resolution simulation of internal wave attractors and impact of interaction of high amplitude internal waves with walls on dynamics of wave attractors. In *Proc. VII European Congress on Computational Methods in Applied Sciences and Engineering*. Crete Island, Greece, 5–10 June 2016, pp. 1–8. National Technical University of Athens.

SUTHERLAND, B. R. 2010 *Internal Gravity Waves*. Cambridge University Press.

SWART, A. 2007 Internal waves and the poincaré equation. PhD thesis, Utrecht University.

SWART, A., MANDERS, A., HARLANDER, U. & MAAS, L. R. M. 2010 Experimental observation of strong mixing due to internal wave focusing over sloping terrain. *Dyn. Atmos. Oceans* **50**, 16–34.

SWART, A., SLEIJPEN, G. L. G., MAAS, L. R. M. & BRANDTS, J. 2007 Numerical solution of the two-dimensional Poincaré equation. *J. Comput. Appl. Maths* **200**, 317–341.

TABAEI, A. & AKYLAS, T. R. 2003 Nonlinear internal gravity wave beams. *J. Fluid Mech.* **482**, 141–161.

TANG, W. & PEACOCK, T. 2010 Lagrangian coherent structures and internal wave attractors. *Chaos* **20**, 017508.

THOMAS, N. H. & STEVENSON, T. N. 1973 An internal wave in a viscous ocean stratified by both salt and heat. *J. Fluid Mech.* **61**, 301–1304.

TROITSKAYA, S. 2017 Mathematical analysis of inertial waves in rectangular basins with one sloping boundary. *Stud. Appl. Maths* **139** (3), 434–456.

VASILIEV, A. Y. & CHASHECHKIN, Y. D. 2003 Generation of 3d periodic internal wave beams. *Z. Angew. Math. Mech.* **67**, 397–405.

VOISIN, B. 2003 Limit states of internal wave beams. *J. Fluid Mech.* **496**, 243–293.

WANG, G., ZHENG, Q., LIN, M., DAI, D. & QIAO, F. 2015 Three dimensional simulation of internal wave attractors in the Luzon Strait. *Acta Oceanol. Sin.* **34**, 14–21.

WUNSCH, C. & FERRARI, R. 2004 Vertical mixing, energy, and the general circulation of the oceans. *Annu. Rev. Fluid Mech.* **36**, 281–314.